Three-dimensional wake transition behind an elliptic cylinder near a moving wall

Jianxun Zhu (朱建勋),[1, a] Fengjian Jiang (蒋奉兼),[2] and Lars Erik Holmedal[1]

[1)] *1. Department of Marine Technology, Norwegian University of Science and Technology, 7052, Trondheim, Norway*

[2)] *2. SINTEF Ocean, 7052, Trondheim, Norway*

(Dated: 24 March 2021)

Three-dimensional flow past an elliptic cylinder with an aspect ratio of 0.5 near a moving bottom wall is investigated numerically for gap ratios of $G/D = 0.1, 0.2, 0.3$ and 0.4 (where G denotes the gap between the cylinder bottom and the moving wall and D is the major-axis length of the cylinder) with Reynolds numbers (*Re*) ranging from 100 to 200 (based on a constant inlet velocity and the major-axis length of the cylinder); the transition between two- and three-dimensional flow regimes is described in detail. For $G/D = 0.4$, the flow is first two-dimensional with a Kármán vortex street followed by a two-layered wake, then it evolves into a three-dimensional flow regime with near-wake and far-wake elliptic instabilities of vortex pairs; for $Re \geq 180$, the near-wake elliptic instability disappears (i.e., the near wake becomes two-dimensional) while the far-wake elliptic instability persists. For $G/D = 0.3$, the flow is first two-dimensional without the development of the two-layered wake, then it evolves into a three-dimensional flow regime with streamwise vorticity pairs propagating periodically in the spanwise direction; this propagation becomes irregular for $Re \geq 160$. For $G/D = 0.2$ the flow is first two-dimensional as for $G/D = 0.3$, then it becomes three-dimensional, exhibiting a behavior of modified mode C instability; for $Re \geq 140$, this flow exhibits a chaotic behavior. For $G/D = 0.1$, the flow is first three-dimensional and steady without vortex shedding, and then develops into an unsteady flow with a dominating upper shear layer in the near-wake and a chaotic wake structure farther downstream.

[a)]Corresponding author: jianxun.zhu@ntnu.no

I. INTRODUCTION

Steady incoming flow past an isolated circular cylinder has been studied extensively due to its fundamental and practical significance[1]. The flow exhibits a transition from two-dimensional periodic flow to three-dimensional flow via a mode A instability at the Reynolds number around 190[2,3], where the Reynolds number (Re) is based on the free-stream velocity (U) and the cylinder diameter (D). The mode A is characterized by streamwise vorticity pairs with a spanwise length ranging from $3D$ to $4D$. The origin of the mode A instability can be attributed to an elliptic instability of the vortex cores in the near wake[4,5], resembling the elliptic instability of a counter-rotating vortex pair[6]. For Re from 240 to 250, the mode A exhibits a gradual transition to another three-dimensional instability mode, i.e., mode B, which is characterized by streamwise vorticity pairs with a smaller spanwise wavelength ranging from $0.8D$ to $1D$. When $Re > 260$, the mode B structure becomes increasingly disordered[7,8]. Williamson[3] suggested that the mode B instability is associated with an instability in the braid shear layer within the near-wake region. Blackburn and Lopez[9] reported the existence of quasi-periodic modes (using Floquet analysis) with spanwise wavelengths between those of modes A and B. These quasi-periodic modes can be combined to produce either standing or traveling wave modes within the cylinder wake. Blackburn, Marques, and Lopez[10] found standing and traveling wave modes with a spanwise wavelength of approximately $2.4D$ for flow past a circular cylinder for $Re > 377$.

The problem of steady incoming flow past an isolated elliptic cylinder has attracted much less attention than that for the circular cylinder although relevant to engineering applications like heat exchangers[11] and bridge piers[12]. This flow depends on both the aspect ratio (AR) of the elliptic cylinder (defined by the ratio of the semi-minor to semi-major axis length) and the incident angle (defined by the angle between the inlet flow direction and the semi-minor axis) in addition to the Reynolds number based on the free-stream velocity and the semi-major axis length. Experimental results obtained by Radi *et al.*[13] for flow around an elliptic cylinder at zero incident angle, show that three-dimensional instability modes equivalent to mode A and mode B (although with slightly different wavelengths) are present sequentially as Re increases for $AR \in [0.26, 0.72]$. Here the critical Re for the onset of mode A decreases as AR decreases. Interestingly, for $AR = 0.39$ and 0.26, the flow exhibits a transition from a three-dimensional wake to a two-dimensional wake for $Re \in [200, 250]$ and for $Re \in [150, 190]$, respectively. Radi *et al.*[13] and Thompson *et al.*[14] suggested that the upstream movement of the two-layered wake caused by increasing Re suppresses the mode A instability. Moreover, Thompson *et al.*[14] (using Floquet analysis) found that the mode A instability does not occur for $AR = 0.1$ and 0 (flat plate) where the near-wake mode structure is modified by the two-layered wake.

Steady incoming flow past a circular cylinder near a moving bottom wall has been investigated by, e.g., Stewart *et al.*[15] and Rao *et al.*[16], who found that at $G/D = 0.005$ (where G denotes the gap between cylinder bottom and the moving bottom wall) and $Re = 90$, this flow exhibits a three-dimensional steady flow regime prior to the onset of unsteady flow, which is not present for the isolated cylinder. Rao *et al.*[17] found that the critical Re for the onset of the unsteady flow regime increases as G/D increases up to 0.25, while for $G/D \geq 0.3$, three-dimensional wake transition (i.e., mode A instability) occurs after the two-dimensional unsteady flow is formed. Here the critical Re for the onset of mode A was found to first decrease and then increase as G/D

increases. Qualitatively similar behaviors are observed by Jiang *et al.*[18,19]. They also reported that at $G/D = 0.2$, the three-dimensional steady and unsteady flow is triggered by a subharmonic mode, i.e., mode C, which is characterized by the streamwise vorticity pairs changing sign after each vortex shedding period. The formation of this mode is due to the moving wall breaking the wake symmetry (i.e., the wake pattern being reflected about the horizontal center-line of the cylinder after half of the vortex shedding period).

In a previous work of Zhu *et al.*[20], the two-dimensional wake pattern behind an elliptic cylinder near a moving wall has been investigated for $G/D \in [0.1, 5]$ and $Re \leq 150$. At small gap ratios, a significant near-wall effect was found on the wake structures (including the Kármán vortex street and the two-layered wake). However, the near-wall effect on the three-dimensional wake transition behind an elliptic cylinder near a moving wall has not been investigated before. In the present work, a detailed three-dimensional numerical investigations for this flow has been conducted with $AR = 0.5$ for $G/D \in [0.1, 0.4]$ and $Re \in [100, 200]$. Overall, the results show that the flow exhibits different wake transition scenarios with increasing Re for each G/D. The transition between two- and three-dimensional flow regimes via the onset of three-dimensional instability modes such as, e.g., mode A, mode C and traveling wave mode, is described in detail. This flow configuration is important for understanding the basic mechanisms for biological flows[21,22] as well as for engineering applications such as an AUV (Autonomous Underwater Vehicle) moving near seabed. The latter is of great importance for mapping the ocean bathymetry as well as for monitoring subsea structures and collecting both physical data (e.g., wave-induced velocities, current velocities and sediment concentration) and biological data (e.g., fish larvae, plankton and contamination).

II. GOVERNING EQUATIONS

The current paper addresses on the three-dimensional wake transition behind an elliptic cylinder near a moving wall. The incompressible flow with a constant density ρ is governed by the three-dimensional Navier-Stokes equations given as

$$\frac{\partial u_i}{\partial x_i} = 0 \tag{1}$$

$$\frac{\partial u_i}{\partial t} + \frac{\partial u_i u_j}{\partial x_j} = -\frac{1}{\rho}\frac{\partial p}{\partial x_i} + \nu \frac{\partial^2 u_i}{\partial x_j \partial x_j} \tag{2}$$

where the Einstein notation using repeated indices is applied. Here u_i = (u, v, w) and x_i = (x, y, z) for i = 1, 2 and 3, indicate the velocity and Cartesian coordinates, respectively, whilst ν, t and p denote the kinematic viscosity of the fluid, time and pressure, respectively. Numerical simulations have been carried out using OpenFOAM (www.openfoam.org). A second-order finite volume method (FVM) is applied in conjunction with the PISO algorithm[23] for solving equations (1) and (2), similar to the numerical approach used in Jiang *et al.*[8].

A. Computational domain and mesh

Figure 1 shows a sketch of the computational domain and the mesh around the elliptic cylinder. The same computational domain was used by Jiang *et al.*[18] for flow around a circular cylinder near a moving wall. The aspect ratio (AR) of the elliptic cylinder is defined by the minor (a) to major (D) axis length ratio, i.e., $AR = a/D$. In the present work, the aspect ratio is set to be 0.5. The gap ratio is given by G/D, where G is the gap between the moving wall and the cylinder. The Reynolds number is based on the major axis length of the cylinder, i.e., $Re = UD/\nu$. The inlet and outlet boundaries are located at upstream $20D$ and downstream $30D$ of the cylinder center, respectively. The top and bottom boundaries are located at $20D$ and $(G+0.5D)$ away from the cylinder center, respectively. Different spanwise lengths of the computational domain are applied for different G/D, which will be further discussed below.

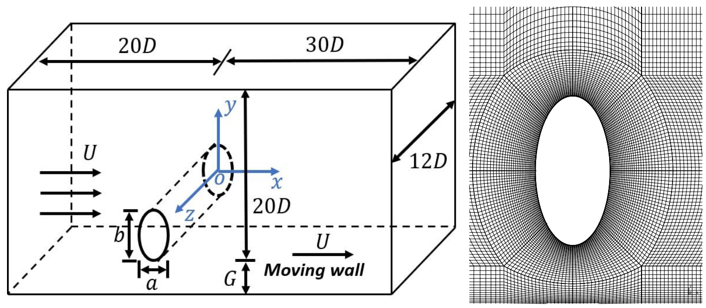

FIG. 1. Sketch of the computational domain and the mesh around the elliptic cylinder.

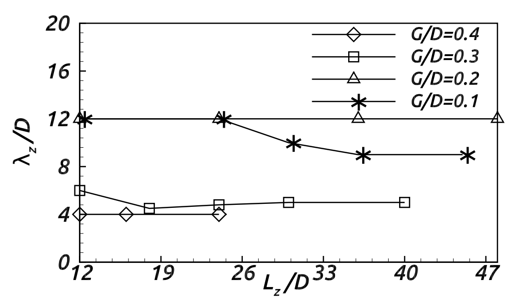

FIG. 2. Variation of the spanwise wavelength (λ_z) of the three-dimensional mode against the spanwise length (L_z) of the computational domain.

As for the boundary conditions, a constant velocity U is set at the inlet while a Neumann condition for the velocity is imposed at the top and outlet boundaries. A no-slip condition is applied at the cylinder surface and the bottom wall, which moves toward the right with a constant velocity U. The pressure is set to be zero at the outlet, and a Neumann condition is imposed at the other boundaries. Periodic boundary conditions are employed in the spanwise ($z-$) direction.

The radial size Δr and vertical size Δy of the first layer of mesh next to the cylinder and the bottom wall, respectively, are set to be the same. A C-type structured mesh[24] is applied around the cylinder. The grid expansion ratio in the whole domain is kept below 1.1, whilst the mesh size (Δz) along the spanwise ($z-$) direction is kept to a constant value. A constant mesh size (Δx) along the x-direction is applied for $x \geq 10D$.

Figure 2 shows simulations for flow around an elliptic cylinder near a moving wall for $G/D \in [0.1, 0.4]$, with different spanwise lengths L_z of the computational domain. It is shown that for $L_z \geq 12D$ (for $G/D = 0.4$), $L_z \geq 30D$ (for $G/D = 0.3$), and $L_z \geq 36D$(for $G/D = 0.2$ and 0.1) the spanwise wavelength λ_z converges to the values $4D$, $5D$, $12D$ and $9D$, respectively. Thus, in the present work, $L_z = 12D$ and $30D$ is applied for $G/D = 0.4$ and 0.3, respectively, and $L_z = 36D$ is applied both for $G/D = 0.2$ and 0.1.

B. Grid independence study

To test grid independence, numerical simulations for flow around an elliptic cylinder of AR = 0.5 near a moving wall have been conducted using three different grid resolutions with $L_z = 12D$ as given in table I for G/D = 0.2 and Re = 200, which represents the most unstable flow regime investigated in the present work. Table I shows the Strouhal number ($St = Df/\nu$, where f is the vortex shedding frequency), time-averaged drag ($\bar{C}_D$) and lift ($\bar{C}_L$) coefficients obtained by three different grid resolutions. The drag and lift coefficients are defined by $C_D = 2F_D/(\rho U^2 L_z D)$ and $C_L = 2F_L/(\rho U^2 L_z D)$, respectively, where F_D and F_L are the drag and lift force on the cylinder, respectively. Here the value of St is almost the same (1000 time units for C_L are included for fast Fourier transform) while $\bar{C}_D$ and $\bar{C}_L$ obtained in case 1 deviate less than 1% from those obtained in case 2 and case 3.

Case	G/D	Re	$\Delta y/\Delta r$	Δz	St	$\bar{C}_D$	$\bar{C}_L$	N (million)
Case 1	0.2	200	0.004	0.2	0.134(±0.001)	1.4966	0.246	3.91
Case 2	0.2	200	0.002	0.2	0.134(±0.001)	1.4832	0.2452	4.11
Case 3	0.2	200	0.004	0.1	0.134(±0.001)	1.4796	0.2443	7.82

TABLE I. Values of the Strouhal number (St), time-averaged drag ($\bar{C}_D$) and lift ($\bar{C}_L$) coefficients for flow around an elliptic cylinder near a moving wall obtained by three different grid resolutions; N denotes the total cell number.

Figure 3 shows almost identical streamwise and spanwise velocity profiles between the cylinder bottom and the bottom wall obtained by three different grid resolutions. Based on the small differences seen in table I and figure 3, we chose to apply the same grid resolution as Case 1 for all numerical simulations in the present work.

C. Validation of the numerical model

A numerical simulation with $L_z = 12D$ for flow around a circular cylinder near a moving wall has been conducted for G/D = 0.4 and Re = 200 using the grid resolution for case 1 to validate the present numerical model. Table II shows the present results and the numerical results previously

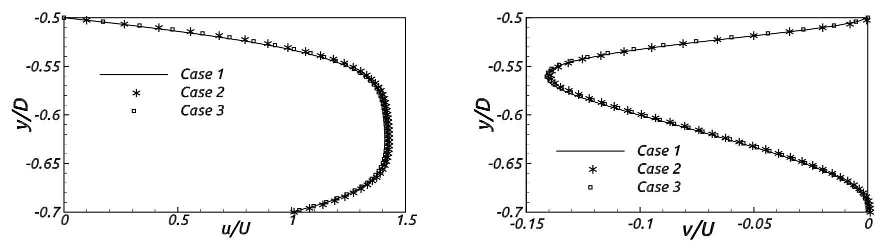

FIG. 3. The streamwise and spanwise velocity profiles between the cylinder bottom and the bottom wall obtained by three different grid resolutions.

reported in Jiang *et al.*[19] for St, $\bar{C}_D$ and the root-mean-square of the lift coefficient (C_L'). Table II shows that St remains almost the same while the deviations of $\bar{C}_D$ and C_L' from the results obtained by Jiang *et al.*[19] are equal to -0.05% and 1.22%, respectively.

Case	G/D	Re	St	$\bar{C}_D$	C_L'
Jiang *et al.*[19]	0.4	200	0.19($\pm$0.001)	1.4742	0.4236
present work	0.4	200	0.19($\pm$0.001)	1.4749	0.4288
Relative difference	-	-	0	-0.05%	1.22%

TABLE II. Values of the Strouhal number (St), time-averaged drag coefficient ($\bar{C}_D$) and root-mean-square of the lift coefficient (C_L') for flow around a circular cylinder near a moving wall for $Re = 200$ with $G/D = 0.4$ using the grid resolution for case 1.

Figure 4 shows the evolution of the wake vortices identified by isosurfaces of λ_2 (left column) and isosurfaces of the streamwise vorticity $\omega_x^*(=\omega_x D/U)$ (right column) for flow around an isolated elliptic cylinder with AR = 0.5 for Re = 115. Here $L_z = 12D$ and λ_2 refers to the method proposed by Jeong and Hussain[25]. The red color of the isosurfaces of λ_2 corresponds to the spanwise vorticity $\omega_z^* = 0.1(=\omega_z D/U)$ whilst the blue color corresponds to $\omega_z^* = -0.1$ due to the vortices shed from the cylinder bottom and top, respectively. At t^* = 300(=tU/D) (figure 4*a*), the wake exhibits a weakly three-dimensional transition as visualized by the isosurfaces of ω_x^* (figure 4*c*) where the black and yellow colors denote the negative and positive values of ω_x^*, respectively. Three streamwise vorticity pairs are formed in the spanwise direction, showing the onset of mode *A* with a spanwise wavelength λ_z of 4D. This wavelength agrees well with the experimental results by Radi *et al.*[13], who found λ_z in the range of 4D to 6D for $AR \in$ [0.39, 0.64]. As the flow develops (t^* = 1000), a vortex dislocation occurs (figure 4*b* and 4*d*), which is qualitatively similar to that observed for flow around an isolated circular cylinder[3,26].

A three-dimensional numerical simulation is conducted for flow around an isolated elliptic cylinder with Re = 110 (not presented here), showing that the wake here remains two-dimensional; the wake becomes three-dimensional at $Re = 115$ (figure 4). Hence the critical Reynolds number (Re_A) for the onset of the mode *A* instability lies between 110 and 115, which is in good agreement with Re_A = 112.2 obtained by Thompson *et al.*[14] for AR = 0.5 using Floquet analysis.

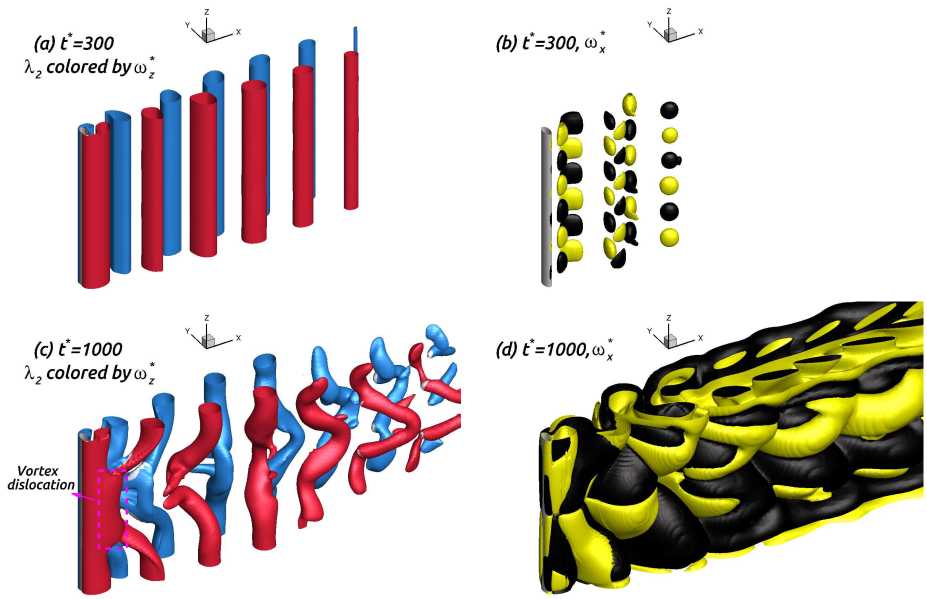

FIG. 4. Instantaneous isosurfaces of λ_2 = -0.05 (left column, colored by $\omega_z^* = \pm 0.1$) and ω_x^*= $\pm$0.005 for flow around an isolated elliptic cylinder of AR = 0.5 for Re = 115 at $t^* = 300$ (*a*-*b*) and $t^* = 1000$ (*c*-*d*).

III. RESULTS AND DISCUSSION

A. Wake transition for configuration with G/D = 0.4

1. *Two-dimensional wake pattern B*

Figure 5 shows a cross-section (in the *xy*-plane) of the ω_z^* contours for Re = 125. Here the wake remains two-dimensional, and the Kármán vortex street exists in the near-wake region; the two-layered wake is developed downstream. The vortices shed from the cylinder bottom disappear earlier than those shed from the cylinder top due to wall suppression effect. This flow is denoted as the two-dimensional wake pattern B, as previously classified by Zhu *et al.*[20].

2. *Modified ordered mode A flow regime*

Figure 6 (Multimedia view) shows the isosurfaces of λ_2 (figures 6*a* and 6*c*) and the corresponding isosurfaces of ω_x^* (figures 6*b* and 6*d*). The near-wake flow remains nearly two-dimensional

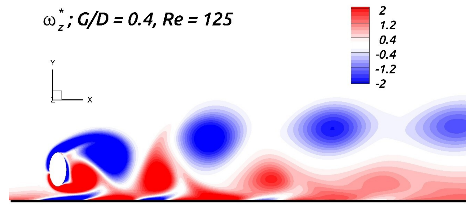

FIG. 5. Contours of ω_z^* at cross-section (x, y, $6D$) for flow around an elliptic cylinder near a moving wall for Re = 125 with G/D = 0.4.

(i.e., no mode A instability) while a span-wise wavy deformation of the vortices shed from the upper part of the cylinder occurs farther downstream at t^* = 200 (figure 6a). Here three streamwise vorticity pairs are observed in the spanwise direction (figure 6b), showing a three-dimensional structure with a wavelength of $\lambda_z = 4D$. It appears that the development of the two-layered wake (visualized by the red and blue λ_2-isosurfaces in figure 6a) leads to the upper vortices moving in a separated layer, with an elliptic instability caused by co-rotating upper vortex pairs[27,28]. This leads to an exponential growth of the spanwise wavy vortex amplitude (H) with time as shown in figure 7. Here the spanwise wavy vortex amplitude is defined by half of the horizontal distance between the trough and crest of the wavy deformation.

As the wake develops with time (see figure 6c and 6d for t^* = 500), the onset location of the wavy deformation of the upper vortices moves upstream towards the cylinder whilst the mode A instability is now present in the near-wake region. This near-wake mode A instability, which is also observed for the isolated elliptic cylinder (figure 4b), can be attributed to the elliptic instability of the counter-rotating vortices shed from the cylinder top and bottom[4,5], respectively. It is worth to note that the vortex dislocation observed for the isolated elliptic cylinder (figure 4b) is not present here since this dislocation is now suppressed by the moving wall. This behavior is qualitatively similar to the observation by Jiang *et al.*[18] for flow around a circular cylinder near a moving wall for $Re \leq 325$ with $G/D < 1$. The flow here is denoted as the modified ordered mode A flow regime, which is different from the ordered mode A flow regime identified by Jiang *et al.*[18] for flow around a circular cylinder near a moving wall where the elliptic instability caused by the co-rotating vortex pairs does not occur in the far-wake region.

Figures 6(e) and 6(f) show ω_x^*-contours in the xz-plane at $y = -0.5D$, corresponding to the ω_x^*-isosurfaces in figure 6(b) and 6(d), respectively. At $t^* = 200$, the strong vorticity pairs lined in the spanwise direction are observed in the far-wake region while these vorticity pairs become stronger in the near-wake region as the wake develops ($t^* = 500$). This behavior coincides with the observations from the isosurfaces of λ_2 and ω_x^* shown in figure 6(a)-6(d).

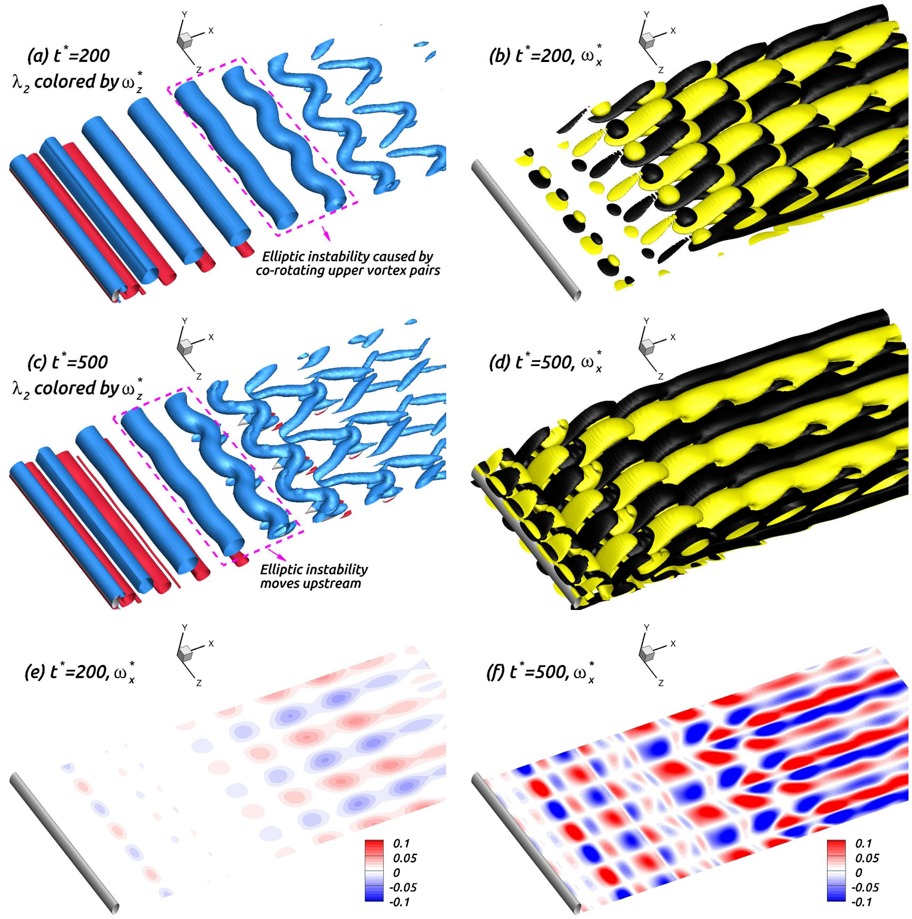

FIG. 6. Isosurfaces (Multimedia view) of λ_2 = -0.05 (colored by ω_z^*; *a* and *c*) and $\omega_x^* = \pm 0.02$ (*b* and *d*) as well as contours of ω_x^* (*e* and *f*) at cross-section $(x, -0.5D, z)$ for flow around an elliptic cylinder of AR = 0.5 for Re = 170 with G/D = 0.4.

3. Near-wake two-dimensional flow regime

As Re increases to 180 (figure 8*a*-8*b*; Multimedia view), the far-wake elliptic instability caused by the upper co-rotating vortex pairs persists while the near-wake flow becomes two-dimensional. This flow is denoted the 'near-wake two-dimensional' flow regime. It is worth to mention that Radi *et al.*[13] reported similar observations for flow around an isolated elliptic cylinder with $AR = 0.26$ for $Re \in [150, 190]$ and with $AR = 0.39$ for $Re \in [200, 250]$. It was suggested by Radi *et al.*[13] and Thompson *et al.*[14] that this might be due to the two-layered wake moving upstream as Re increases

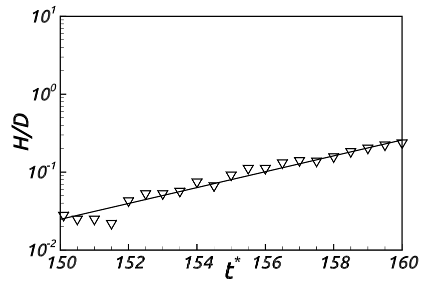

FIG. 7. Time history of the amplitude for one vortex centerline oscillation for flow around an elliptic cylinder near a moving wall for Re = 170 with G/D = 0.4.

(for a given AR) or as AR decreases (for a given Re), thus suppressing the mode A instability in the near-wake region. In the present work, the near-wall effect leads to the two-layered wake moving upstream, thus suppressing the near-wake instability. This upstream movement of the two-layered wake caused by the near-wall effect was previously demonstrated by Zhu *et al.*[20] for two-dimensional flow past an elliptic cylinder near a moving wall.

As a comparison, a simulation of flow around a circular cylinder near a moving wall is conducted for Re = 180 and G/D = 0.4. The resulting isosurfaces of λ_2 and ω_x^* are shown in figures 8(c)-8(d), respectively. Here the two-layered wake is absent and the flow exhibits the mode A instability in the near-wake region. This gives further support to the hypothesis of the near-wake being suppressed by the two-layered wake moving upstream towards the cylinder due to the effect of the bottom wall.

B. Wake transition for configuration with G/D = 0.3

Numerical simulations show that the critical Re for the onset of the three-dimensional wake instability lies between 145 and 150, which is larger than the corresponding critical Re (125-135) for $G/D = 0.4$. This trend was also observed by Jiang *et al.*[18] for flow around a circular cylinder near a moving wall as G/D was decreased from 0.4 to 0.3.

1. Two-dimensional wake pattern C

Figure 9 shows a cross-section (in the xy-plane) of the ω_z^* contours for Re = 145. The flow here is two-dimensional, exhibiting the wake pattern C, which is characterized by pair-wise vortex shedding without the development of the two-layered wake[20].

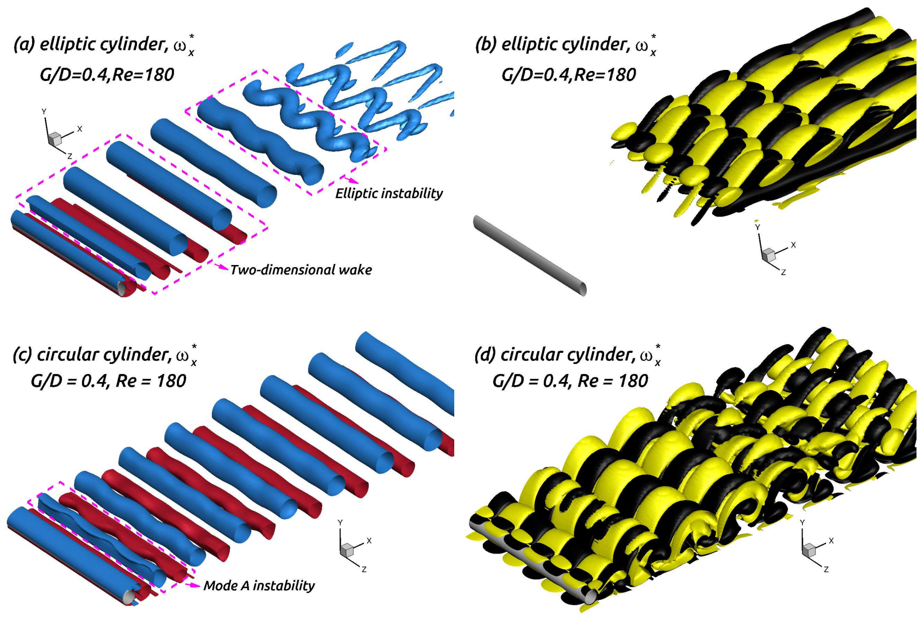

FIG. 8. Isosurfaces (Multimedia view) of λ_2 = -0.05 (left column, colored by ω_z^*) and $\omega_x^* = \pm 0.02$ (right column) for flow around an elliptic cylinder of AR = 0.5 (*a*-*b*) and circular (*c*-*d*) cylinder for Re = 180 with G/D = 0.4.

2. *Traveling wave mode flow regime*

As Re increases to 150, a quasiperiodic three-dimensional mode, i.e., the traveling wave mode[9,10], occurs. This mode is characterized by a spanwise propagation of the wavy deformation of the vortices (as visualized by λ_2-isosurfaces in figure 10*a* and 10*c*), coinciding with the streamwise vorticity pairs with oblique alternating streamwise vorticies (as visualized by ω_x^*-isosurfaces in figure 10*b*, 10*d*, 10*e* and 10*f*) for Re = 150 and G/D = 0.3. Here T denotes the vortex shedding period. At t^* = t_0 (=2403) the six crests of the wavy deformation (figure 10*a*), corresponding to the six streamwise vorticity pairs (figure 10*b*), show each streamwise vortex pair (marked as TW mode) exhibits a length of $\lambda_z = 5D$. These streamwise vortex pairs propagate in the positive z-direction (see figure 10*d*-10*e*; from $t^* = t_0 + T$ to $t^* = t_0 + 2T$). After eight vortex shedding periods (figure 10*f*), the pattern starts to repeat itself. This process can be further illustrated by ω_x sampled along the z-direction at the location $x = 0.4D$ and $y = 0.6D$ (figure 11*a*), showing that the streamwise vorticity pairs move in the positive z-direction with a nearly constant distance for each vortex shedding period. After eight vortex shedding periods, the streamwise vorticity pairs are identical to those at t^*=t_0 in terms of both position and amplitude.

As Re increases to 155 (figure 11*b*), the streamwise vorticity pairs propagate in the positive z-direction with different distances per cycle, but still nearly repeat themselves after eight vortex

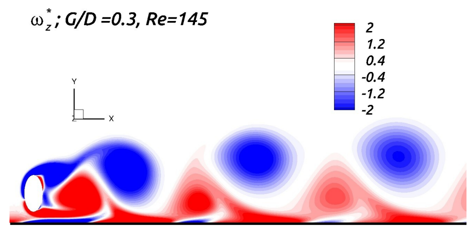

FIG. 9. Contours of ω_z^* at cross-section (x, y, $15D$) for flow around an elliptic cylinder near a moving wall for Re = 145 with G/D = 0.3.

shedding cycles with a slightly smaller amplitude. It should be noted that the crests (indicating the positive values of ω_x^*) are wider while the troughs (indicating the negative values of ω_x^*) are sharper. It appears that the wake becomes more unsteady such that the streamwise vortex pair become imbalanced in strength. The flow here which is $8T$-periodic is denoted as the 'traveling wave (TW) mode' flow regime.

3. *Squiggly wave traveling mode flow regime*

Figure $11(c)$ shows ω_x^* sampled along a line in the spanwise direction for $x = 0.4D$ and $y = 0.6D$ for Re = 160. Here the streamwise vorticity pairs propagate in the positive z-direction but with different propagation distances for each vortex shedding period (see, e.g., the propagation distances from t^* = t_0 (=3401) to t_0+T and from t^* = t_0+T to t_0+$2T$). Here ω_x^* exhibits a more 'nonlinear' behavior (relative to the more sinusoidal behavior observed in figure 11a and 11b) and does not repeat itself after $8T$. The flow here is slightly more irregular than the 'traveling wave mode' flow regime, thus denoted as the squiggly wave traveling mode' flow regime.

Overall, as Re increases from 100 to 200, the flow exhibits a transition scenario of 'two-dimensional wake pattern C' $\rightarrow$ 'traveling wave (TW) mode flow regime' $\rightarrow$ 'squiggly traveling wave (TW) mode flow regime'.

C. Wake transition for configuration with $G/D = 0.2$

Numerical simulations conducted by the authors (not presented here) show that for $Re \leq 120$, the flow is two-dimensional without vortex shedding. As Re increases to 121, a transition to the two-dimensional wake pattern C occurs while the three-dimensional instability occurs at $Re = 122$.

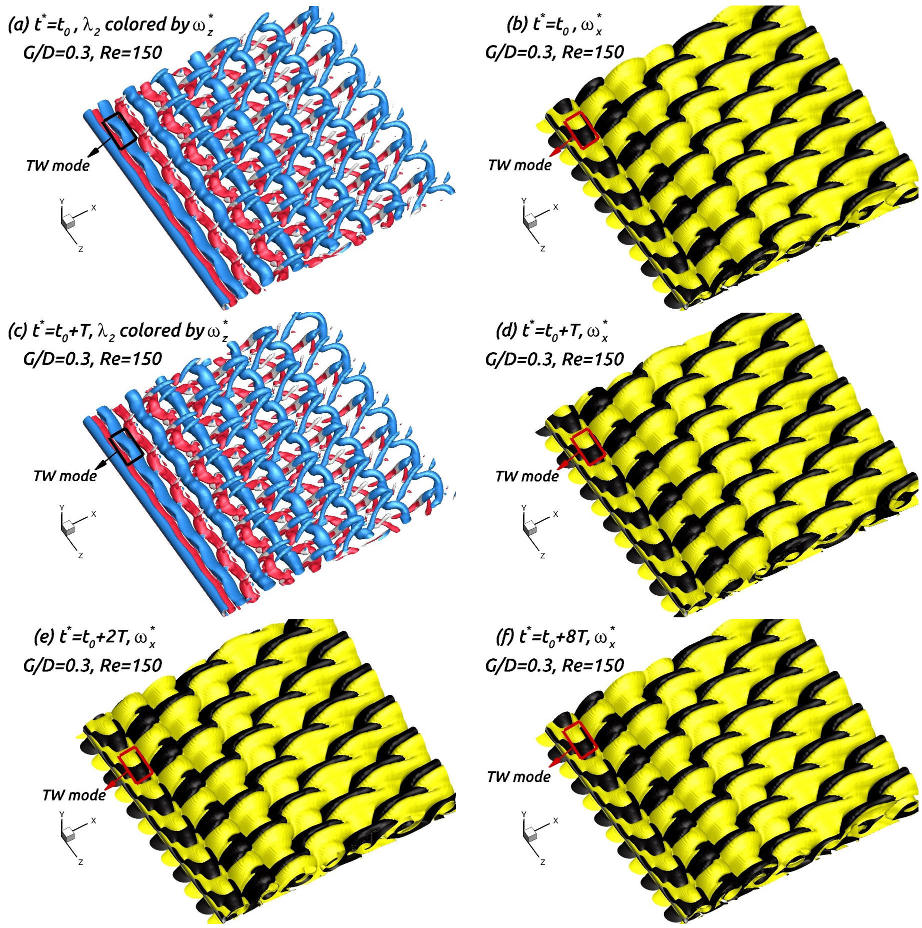

FIG. 10. Isosurfaces (Multimedia view) of λ_2 = -0.05 (*a* and *c*, colored by ω_z^*) and $\omega_x^* = \pm 0.02$ (*b*, *d*, *e* and *f*) for flow around an elliptic cylinder near a moving wall for *Re* = 150 at G/D = 0.3. T denotes the vortex shedding period.

1. *Modified mode C flow regime*

The presence of the moving wall close to the elliptic cylinder leads to the wake symmetry being broken, resulting in the mode C instability[29,30], as described in detail in the introduction. Jiang *et al.*[18] found that the mode *C* structure is strongly affected by the shear layer developed on the moving wall. In order to investigate the pure mode *C* structure, a numerical simulation with a slip condition imposed on the bottom wall (implying no shear layer developed on the bottom wall) has been conducted for *Re* = 125 and G/D = 0.2. As visualized by isosurfaces of ω_x^* shown in figure

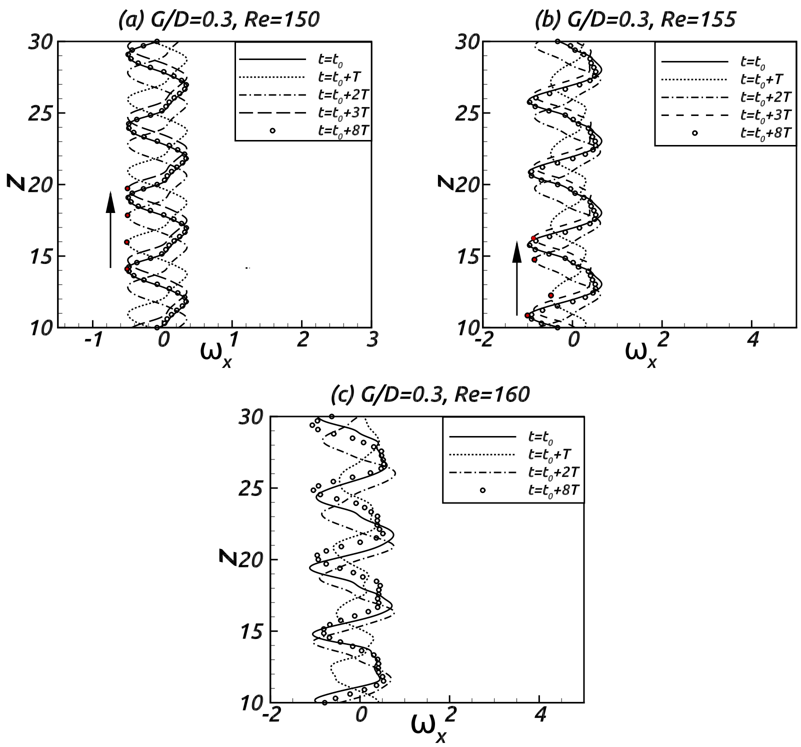

FIG. 11. Values of ω_x^* sampled at (0.4D, 0.6D, z) for flow around an elliptic cylinder near the moving wall for Re = (a) 150, (b) 155 and (c) 160 at G/D = 0.3.

12, the features of the mode C structure is present; the streamwise vorticity with $\lambda_z = 2.6D$ (figure 12a; $t_0 = 1000$) changes sign after one vortex shedding period (figure 12b) and repeat itself after two shedding periods (figure 12c). This is consistent with the results obtained by Jiang *et al.*[18] for flow around a circular cylinder near a slip wall at $G/D = 0.2$ for $Re = 140$. Mode C also triggers the three-dimensional instability for flow around an elliptic cylinder near a moving wall as visualized by the isosurfaces of λ_2 and ω_x^* in figure 13 for $Re = 125$ and $G/D = 0.2$ at $t^* = 100$. The spanwise wavelength of the mode C is approximately equal to 1.5D, which is smaller than that ($\lambda_z = 2.6D$) obtained for the slip wall condition as shown in figure 12.

Figure 14 (Multimedia view) shows the isosurfaces of λ_2 from $t^* = t_0$ (= 2650) to $t_0 + 5T$. Here the wavy deformation of the vortices ($t^* = t_0$) shows the mode C structures evolving into streamwise vortices with a wavelength of $\lambda_z = 12D$. This behavior can be further visualized by the corresponding ω_x^* sampled along a line in the spanwise direction for $x = 2D$ and $y = 0.55D$ shown in figure 15. The wavy deformation of the vortices persists for the next vortex shedding period (in figure 14b) but with a small decrease around the peak value of ω_x^* (figure 15 for t^*

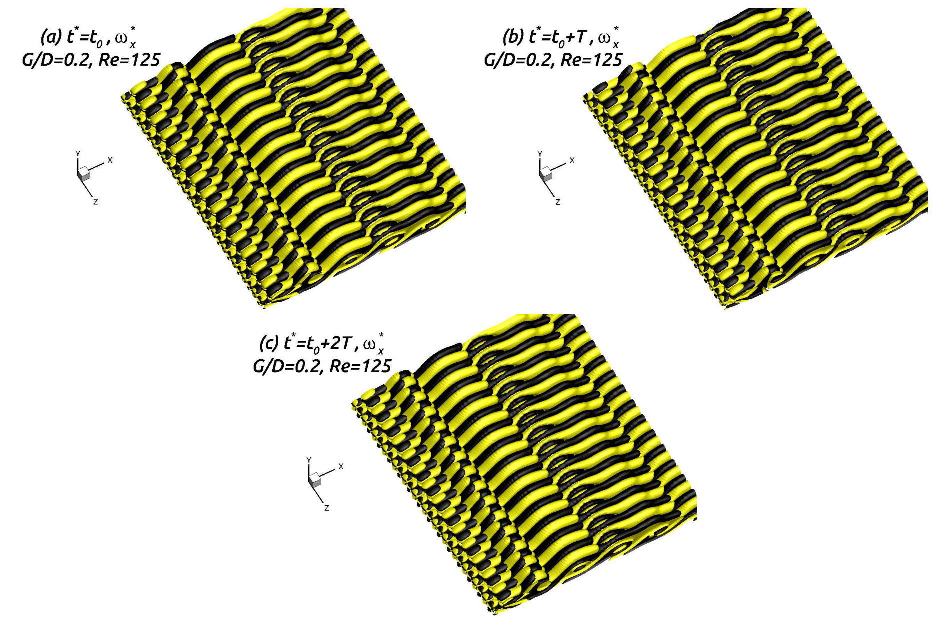

FIG. 12. Isosurfaces of $\omega_x^* = \pm 0.01$ for flow around an elliptic cylinder near a slip wall for $Re = 125$ with $G/D = 0.2$ at $t^* = (a)\, t_0, (b)\, t_0 + T$ and $(c)\, t_0 + 2T$.

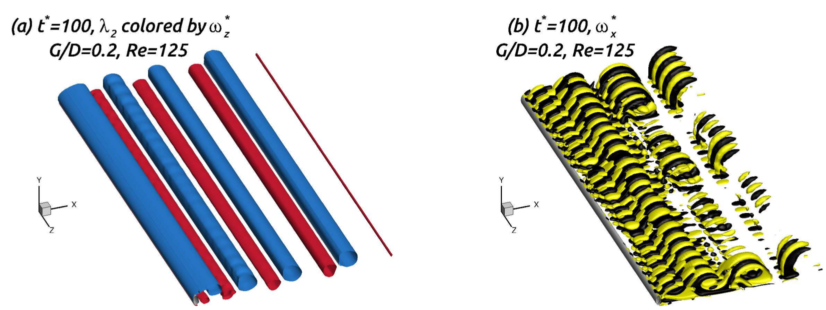

FIG. 13. Isosurfaces of (a) λ_2 = -0.05 (colored by ω_z^*) and (b) ω_x^* = $\pm$0.01 for flow around an elliptic cylinder of $AR = 0.5$ for $Re = 125$ at $G/D = 0.2$.

= t_0+T). In the next vortex shedding period (figure 15c), the wavy deformation of the shedding vortex nearly disappears, indicating a decay of the three-dimensional instability within this period, coinciding with the small value of ω_x^* observed in figure 15 at the same time instant (t^* =t_0+2T). Interestingly, the three-dimensional instability re-occurs for the next vortex shedding period (figure 14d) but the value of ω_x^* is now opposite of that for $t^* = t_0$ and $t_0 + T$ as shown in figure 15. The

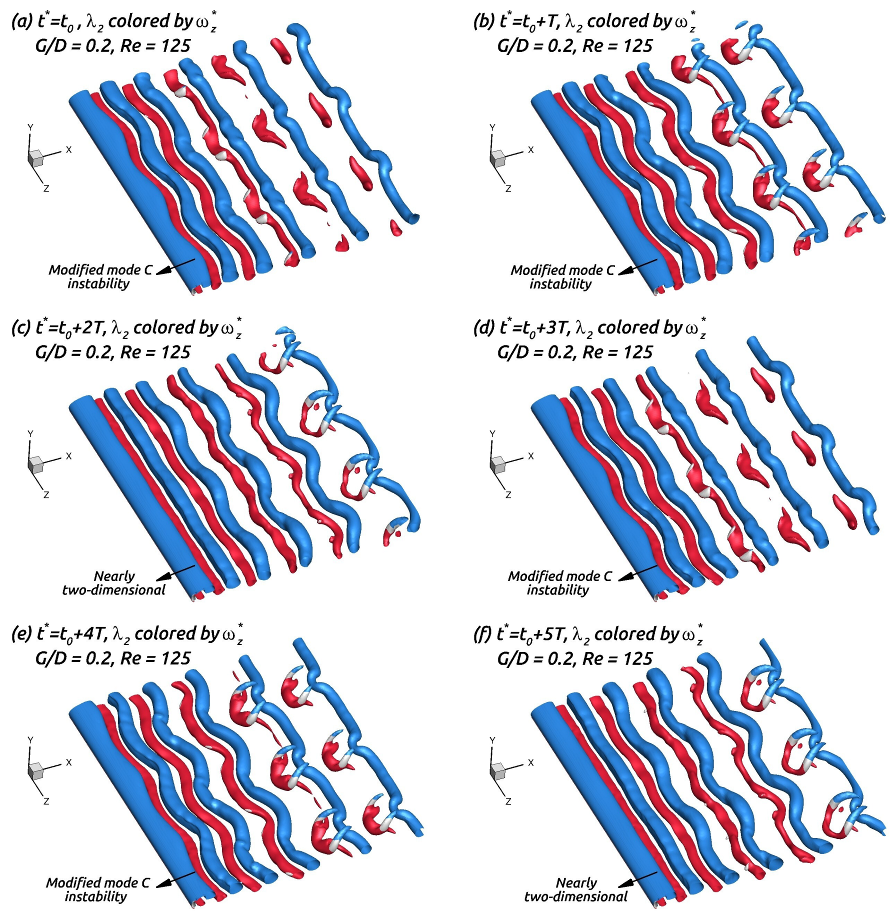

FIG. 14. Isosurfaces (Multimedia view) of λ_2 = -0.05 (colored by ω_z^*) for flow around an elliptic cylinder of AR = 0.5 for Re = 125 with G/D = 0.2 at $t^* = (a)\, t_0, (b)\, t_0+T, (c)\, t_0+2T, (d)\, t_0+3T, (e)\, t_0+4T$ and $(f)\, t_0+5T$. T denotes the vortex shedding period.

behavior observed for $[t_0,\, t_0+2T]$ is repeated for $[t_0+3T,\, t_0+5T]$ as shown in figures 14 and 15. After one further vortex shedding period (t^* = t_0+6T), the streamwise voriticity pairs repeat themselves, i.e., the ω_x^* profiles at t^* = t_0 and t^* = t_0+6T coincide as shown in figure 15. This flow is denoted as the modified mode C flow regime. It appears that the interruption of mode C here is due to the bottom-wall shear layer since a pure mode C structure persists when a slip wall condition is applied (figure 12).

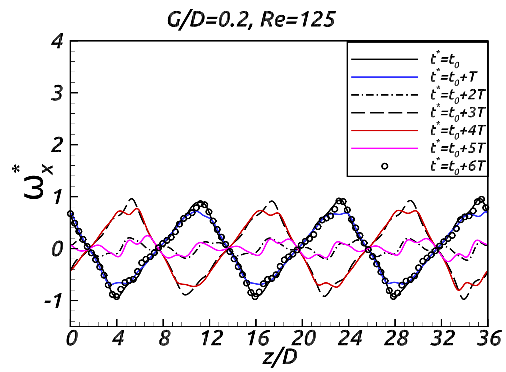

FIG. 15. Values of ω_x^* sampled at (2.0D, 0.55D, z) for flow around an elliptic cylinder near the moving wall for Re = 125 with G/D = 0.2.

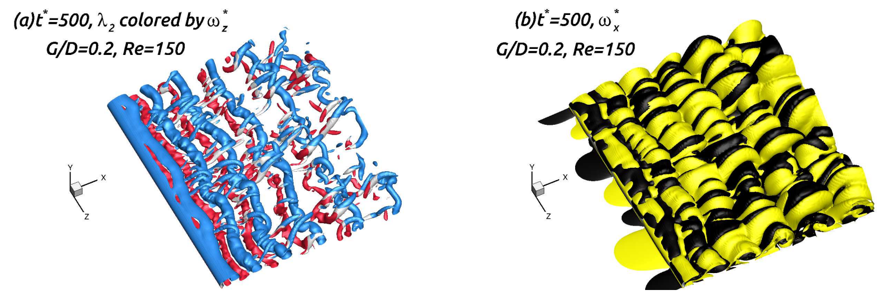

FIG. 16. Isosurfaces of (a) λ_2 = -0.05 (colored by ω_z^*) and (b) ω_x^* = ±0.01 for flow around an elliptic cylinder for Re = 150 with G/D = 0.2.

2. *Chaotic flow regime*

Figure 16 shows isosurfaces of λ_2 and ω_x^* for $Re = 150$. Here the wake becomes chaotic with an irregular wavy deformation of the shedding vortex (figure 16a), corresponding to streamwise vorticities with a range of different spanwise wavelengths λ_z (figure 16b). This flow is denoted as the chaotic flow regime.

D. Wake transition for configuration with G/D = 0.1

1. *Three-dimensional steady flow regime*

Figure 17 shows time-history of the spanwise velocity sampled at $(x, y, z) = (0.5D, 0.5D, 18D)$ (i.e., in the wake) and isosurfaces of ω_x^* for $Re = 100$ and $G/D = 0.1$. The spanwise velocity (figure 17*a*) becomes constant after $t^* = 2500$, indicating the evolution of the flow towards the three-dimensional steady flow regime. Four streamwise vorticity pairs (figure 17*b*) are present along the cylinder in the spanwise direction, corresponding to a spanwise wavelength of $\lambda_z = 9D$, which is larger than that $\lambda_z = 6D$ observed in the three-dimensional steady flow regime for a circular cylinder near a moving wall[13,18] for $G/D \leq 0.22$. It should be noted that this flow regime does not occur for flow around an elliptic cylinder at $G/D = 0.2$ because the critical G/D for the onset of the unsteady flow is larger for an elliptic cylinder than for a circular cylinder[20].

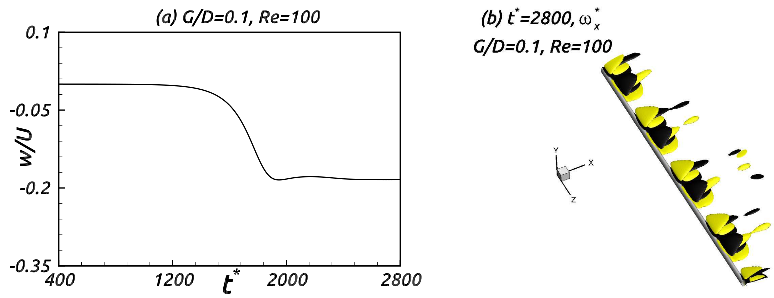

FIG. 17. (a) the time history of the spanwise velocity w sampled at (0.5D, 0.5D, 18D) and (b) isosurfaces of $\omega_x^* = \pm 0.17$ for flow around an elliptic cylinder near a moving wall for Re = 100 with G/D = 0.1.

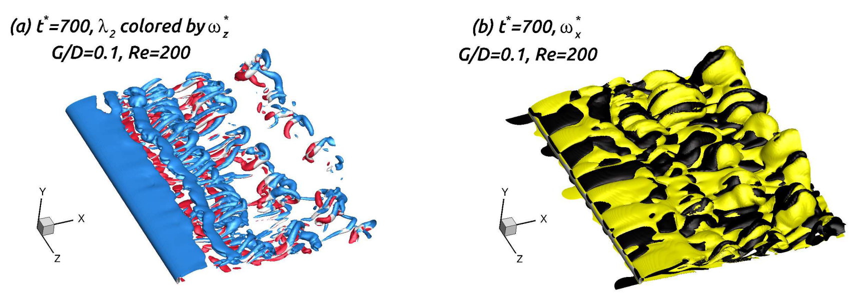

FIG. 18. Isosurfaces (Multimedia view) of (a) λ_2 = -0.05 (colored by ω_z^*) and (b) $\omega_x^* = \pm 0.01$ for flow around an elliptic cylinder near a moving wall for Re = 200 with G/D = 0.1.

2. *Three-dimensional wake pattern D*

Figure 18 (Multimedia view) shows the isosurfaces of λ_2 and ω_x^* for Re = 200. Here the flow exhibits a dominating upper shear layer behind the cylinder (shown by the blue contours in figure 18*a*) and a chaotic streamwise vorticity pattern farther downstream (figure 18*b*). Figure 19 shows that C_D and C_L are nearly constant in time. This behavior is qualitatively similar to that observed for wake pattern D identified by Zhu *et al.*[20] for two-dimensional flow. Thus, this flow, depicted in figure 18, is denoted as the three-dimensional wake pattern D.

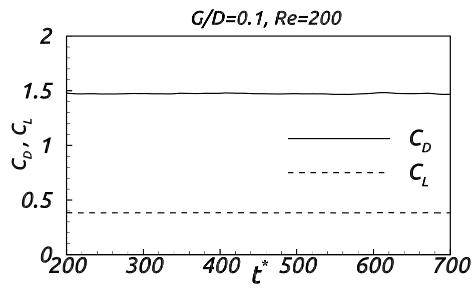

FIG. 19. Time history of drag and lift coefficients for flow around an elliptic cylinder near a moving wall for Re = 200 with G/D = 0.1.

IV. SUMMARY AND CONCLUSIONS

In this paper, numerical simulations have been conducted for flow around an elliptic cylinder with an aspect ratio AR of 0.5 near a moving wall for $G/D \in [0.1, 0.4]$ and $Re \in [100, 200]$. Here four configurations with $G/D = 0.1, 0.2, 0.3$ and 0.4 are investigated. Different wake transition scenarios have been observed for each configuration. Table III summarizes how the wake patterns change with Re for each G/D configuration.

G/D =0.4	G/D =0.3
Wake pattern B ($Re \leq 125$)	Wake pattern C ($Re \leq 145$)
Modified mode A ($Re \in [135, 170]$)	TW mode ($Re \in [150, 155]$)
Near-wake two-dimensional ($Re \geq 180$)	Squiggly TW mode ($Re \geq 160$)

G/D =0.2	G/D =0.1
Two-dimensional steady ($Re \leq 120$)	Three-dimensional steady ($Re = 100$)
Wake pattern C ($Re = 121$)	Wake pattern D' ($Re \geq 125$)
Modified mode C ($Re \in [122, 130]$)	-
Chaotic ($Re \geq 140$)	-

TABLE III. Different flow regimes for flow around a circular cylinder near a moving wall for $Re \in [100, 200]$ and $G/D \in [0.1, 0.4]$. TW mode denotes the traveling wave mode[10]. Wake patterns B, C and D' denote two-dimensional wake pattern B and C identified by Zhu *et al.*[20], and three-dimensional wake pattern, qualitatively similar to two-dimensional wake pattern D[20], respectively.

The wake transition scenario for $G/D = 0.4$ can be summarized as follows: For $Re \leq 120$, the flow is two-dimensional, exhibiting wake pattern B, which is characterized by a Kármán vortex street in the near-wake region and a two-layered wake developed farther downstream. For $Re \in [135, 170]$, the flow becomes three-dimensional, exhibiting the modified ordered mode A flow regime where an elliptic instability (mode A instability) of counter-rotating vortex pairs (i.e., vortices shed from the cylinder top and bottom, respectively) occurs in the near-wake region whilst an elliptic instability of co-rotating upper vortex pairs is present farther downstream due to the development of the two-layered wake with the upper vortices moving in a separated layer. For $Re \in [180, 200]$, the flow becomes two-dimensional in the near-wake region while the elliptic instability caused by the co-rotating upper vortices persists in the far-wake region. The reason for the two-dimensional near-wake flow appears to be that the two-layered wake moves upstream towards the cylinder as Re increases, suppressing the near-wake mode A instability which is present for $Re \in [135, 170]$.

For $G/D = 0.3$, the following wake transitions take place: For $Re \leq 145$, the flow is two-dimensional, exhibiting wake pattern C, which is characterized by pair-wise vortex shedding without the development of the two-layered wake. For $Re \in [150, 155]$, a three-dimensional instability occurs, forming the traveling wave mode flow regime characterized by a spanwise propagation of the streamwise vorticity pairs with oblique alternating streamwise vorticies. This flow repeat itself after 8 vortex shedding periods. For $Re \in [160, 200]$, the flow becomes more irregular, exhibiting the squiggly traveling wave mode flow regime where the spanwise progation of the streamwise vorticity pairs persists but with different propagation distances for each vortex shedding period.

For $G/D = 0.2$, the following wake transitions are found: For $Re \leq 120$, the flow is two-dimensional and steady without vortex shedding. For $Re = 121$, the flow exhibits the two-dimensional wake pattern C, as described in the paragraph above. For $Re \in [122, 130]$, the flow becomes three-dimensional, exhibiting the modified mode C flow regime where the wavy deformation of the shedding vortices is kept for two vortex shedding periods, and then disappears in the next shedding period. This behavior is repeated for the next three vortex shedding periods but with an opposite wavy deformation direction; the flow repeats itself after six vortex shedding periods. For $Re \geq 140$, the wake becomes chaotic with an irregular wavy deformation of the shedding vortices.

For $G/D = 0.1$, one wake transition takes place as follows: For $Re = 100$, the flow is three-dimensional and steady without vortex shedding, containing a constant spanwise velocity within the wake; for $Re \in [125, 200]$, the flow becomes unsteady, exhibiting the three-dimensional wake pattern D, which is characterized by a dominating upper shear layer behind the cylinder, followed by a chaotic wake structure farther downstream. Here the drag (C_D) and lift (C_L) coefficients are nearly time-independent.

ACKNOWLEDGEMENTS

We gratefully acknowledge the support for this research from the Department of Marine Technology, Norwegian University of Science and Technology.

DATA AVAILABILITY

The data that support the findings of this study are available from the corresponding author upon reasonable request.

REFERENCES

[1] B. Sumer and J. Fredsøe, *Hydrodynamics around cylindrical strucures*, Vol. 26 (World Scientific, 2006).

[2] D. Barkley and R. Henderson, "Three-dimensional floquet stability analysis of the wake of a circular cylinder," Journal of Fluid Mechanics **322**, 215–241 (1996).

[3] C. Williamson, "Three-dimensional wake transition," Journal of Fluid Mechanics **328**, 345–407 (1996).

[4] T. Leweke and C. Williamson, "Three-dimensional instabilities in wake transition," European Journal of Mechanics-B/Fluids **17**, 571–586 (1998).

[5] M. Thompson, T. Leweke, and C. Williamson, "The physical mechanism of transition in bluff body wakes," Journal of Fluids and Structures **15**, 607–616 (2001).

[6] T. Leweke and C. Williamson, "Cooperative elliptic instability of a vortex pair," Journal of Fluid Mechanics **360**, 85–119 (1998).

[7] C. Williamson, "Vortex dynamics in the cylinder wake," Annual Review of Fluid Mechanics **28**, 477–539 (1996).

[8] H. Jiang, L. Cheng, S. Draper, H. An, and F. Tong, "Three-dimensional direct numerical simulation of wake transitions of a circular cylinder," Journal of Fluid Mechanics **801**, 353 (2016).

[9] H. Blackburn and J. Lopez, "On three-dimensional quasiperiodic Floquet instabilities of two-dimensional bluff body wakes," Physics of Fluids **15**, L57–L60 (2003).

[10] H. Blackburn, F. Marques, and J. Lopez, "Symmetry breaking of two-dimensional time-periodic wakes," Journal of Fluid Mechanics **522**, 395–411 (2005).

[11] W. Khan, J. Culham, and M. Yovanovich, "Fluid flow around and heat transfer from elliptical cylinders: analytical approach," Journal of Thermophysics and Heat Transfer **19**, 178–185 (2005).

[12] B. Jensen, S. Carstensen, and E. Christensen, "Mixing of stratified flow around bridge piers in steady current," Journal of Hydraulic Engineering **144**, 04018041 (2018).

[13] A. Radi, M. Thompson, J. Sheridan, and K. Hourigan, "From the circular cylinder to the flat plate wake: the variation of Strouhal number with Reynolds number for elliptical cylinders," Physics of Fluids **25**, 101706 (2013).

[14] M. Thompson, A. Radi, A. Rao, J. Sheridan, and K. Hourigan, "Low-Reynolds-number wakes of elliptical cylinders: from the circular cylinder to the normal flat plate," Journal of Fluid Mechanics **751**, 570–600 (2014).

[15] B. Stewart, M. Thompson, T. Leweke, and K. Hourigan, "The wake behind a cylinder rolling on a wall at varying rotation rates," Journal of Fluid Mechanics **648**, 225 (2010).

[16] A. Rao, B. Stewart, M. Thompson, T. Leweke, and K. Hourigan, "Flows past rotating cylinders next to a wall," Journal of Fluids and Structures **27**, 668–679 (2011).

[17] A. Rao, M. Thompson, T. Leweke, and K. Hourigan, "The flow past a circular cylinder translating at different heights above a wall," Journal of Fluids and Structures **41**, 9–21 (2013).
[18] H. Jiang, L. Cheng, S. Draper, and H. An, "Two-and three-dimensional instabilities in the wake of a circular cylinder near a moving wall," Journal of Fluid Mechanics **812**, 435–462 (2017).
[19] H. Jiang, L. Cheng, S. Draper, and H. An, "Three-dimensional wake transition for a circular cylinder near a moving wall," Journal of Fluid Mechanics **818**, 260–287 (2017).
[20] J. Zhu, L. Holmedal, D. Myrhaug, and H. Wang, "Near-wall effect on flow around an elliptic cylinder translating above a plane wall," Physics of Fluids **32**, 093607 (2020).
[21] B. Heather, "Seal whiskers inspire marine technology," Oceanus Magazine **51**, 82–85 (2016).
[22] H. Beem and M. Triantafyllou, "Wake-induced 'slaloming' response explains exquisite sensitivity of seal whisker-like sensors," Journal of Fluid Mechanics **783**, 306–322 (2015).
[23] R. Issa, "Solution of the implicitly discretised fluid flow equations by operator-splitting," Journal of Computational Physics **62**, 40–65 (1986).
[24] J. Thompson, B. Soni, and N. Weatherill, *Handbook of Grid Generation* (CRC Press, 1998).
[25] J. Jeong and F. Hussain, "On the identification of a vortex," Journal of Fluid Mechanics **285**, 69–94 (1995).
[26] H. Jiang, L. Cheng, F. Tong, S. Draper, and H. An, "Stable state of mode a for flow past a circular cylinder," Physics of Fluids **28**, 104103 (2016).
[27] P. Meunier and T. Leweke, "Three-dimensional instability during vortex merging," Physics of Fluids **13**, 2747–2750 (2001).
[28] T. Leweke, S. Le Dizès, and C. Williamson, "Dynamics and instabilities of vortex pairs," Annual Review of Fluid Mechanics **48**, 507–541 (2016).
[29] G. Sheard, M. Thompson, and K. Hourigan, "Subharmonic mechanism of the mode c instability," Physics of Fluids **17**, 111702 (2005).
[30] H. Blackburn and G. Sheard, "On quasiperiodic and subharmonic floquet wake instabilities," Physics of Fluids **22**, 031701 (2010).